PHYSICAL REVIEW B VOLUME 21, NUMBER 11 1 JUNE 1980

Structural transitions between epitaxially ordered phases in adsorbed submonolayers

S. Ostlund
Department of Physics, Harvard University, Cambridge, Massachusetts 02138

A. N. Berker
Department of Physics, Harvard University, Cambridge, Massachusetts 02138
and Department of Physics, Massachusetts Institute of Technology, Cambridge, Massachusetts 02139*

(Received 17 December 1979)

The global phase diagram of a triangular lattice-gas model for submonolayers adsorbed epitaxially on basal graphite is studied using a position-space renormalization method. This model has nearest-neighbor exclusion, and accomodates dominant third-neighbor interaction. Each cell of 12 sites is mapped onto a single local degree of freedom with a singlet-triplet-quadruplet structure. The lattice gas, with up to 20th-neighbor interactions, is thereby transformed into a nearest-neighbor model, which is then analyzed by a Migdal-Kadanoff renormalization transformation. At low temperatures, as coverage is increased from zero, gas, 2×2 solid, and $\sqrt{3} \times \sqrt{3}$ solid phases can be encountered, separated by first-order transitions. These solids undergo first- or higher-order transitions into fluid phases as temperature is increased at given density. Triple points, multicritical points, and/or critical end-points occur for various relative strengths of interactions. For certain plausible potentials, the 2×2 solid occurs at finite temperature, but not at zero temperature. Distinct liquid and gas phases, with a solid-liquid-gas triple point, are found in some cases. Contact is made with the phase diagram of methane physisorbed on basal graphite, suggesting that the effective hard-core radius of methane is increased by adsorption. A phase diagram very similar to that exhibited by oxygen chemisorbed on nickel (111), with both 2×2 and $\sqrt{3} \times \sqrt{3}$ structures, is also obtained.

I. INTRODUCTION

Renormalization theory calculations[1-3] of the phase diagrams and thermodynamic properties of helium, krypton, and nitrogen submonolayers[4] on graphite have yielded considerable quantitative agreement with experiments.[5-12] The two-dimensional "solid" phase which occurs in these works has an ordered structure determined by the periodicity of the substrate, and is therefore labeled "commensurate" (to the substrate). Specifically, the above systems exhibit a $\sqrt{3} \times \sqrt{3}$ commensurate solid,[10-14] in which the adsorbed molecules preferentially occupy one of three equivalent sublattices formed by the adsorption sites. In the present work, we have been interested in the possibility of different types of commensurate solids[15,16] appearing in the same phase diagram,[17] with intervening structural transitions.[18]

The basal surface of graphite presents a triangular array of preferred adsorption sites, which are the centers of the carbon hexagons. For an adsorbate such as xenon, the minimum in the adatom pair potential[19] occurs near the separation of third-neighbor sites (Fig. 1). At low temperature and chemical potential, the adsorption lattice is essentially empty. Simple ground-state analysis then indicates that as the chemical potential (or, equivalently, the pressure of the gas in the experimental container) is raised, a

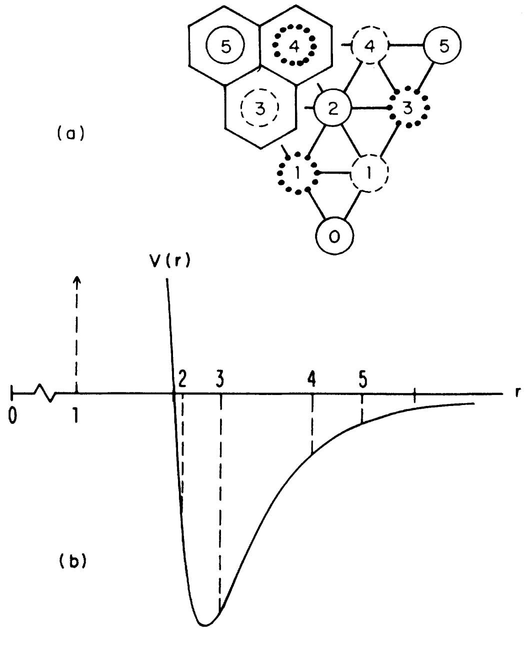

FIG. 1. (a) The hexagonal substrate forms a triangular lattice of adsorption sites. The dashed, dotted, and solid circles show the three sublattices. The neighbors of site 0 are consecutively numbered. (b) The Lennard-Jones potential of xenon on graphite (Ref. 19), with 1–5th-neighbor separations indicated.

solid with a 2×2 unit cell [Fig. 2(a)] appears[20] by a first-order transition. As the chemical potential is raised further, a structural phase transition takes place, in which this 2×2 solid is squeezed into a denser solid with a $\sqrt{3} \times \sqrt{3}$ unit cell [Fig. 2(b)]. Of interest is the finite temperature behavior of this system.

Our calculation is composed of two distinct parts. A lattice gas is considered, with general further-neighbor interactions and nearest-neighbor exclusion, which is appropriate for adsorbates on graphite with hard cores comparable to or larger than that of krypton.[6] In a prefacing transformation,[21] this Hamiltonian is mapped onto a Hamiltonian with somewhat more complicated local degrees of freedom coupled by nearest-neighbor interactions. The ground states of the original system are preserved.[22] The latter system is analyzed using a renormalization-group method.[23,24]

As shown in Fig. 2(a), the triangular lattice of adsorption sites can be decomposed into four equivalent sublattices, one of which is preferentially occupied in the 2×2 solid. The adsorption lattice can also be decomposed into three equivalent sublattices, one of which is preferentially occupied in the $\sqrt{3} \times \sqrt{3}$ solid [Fig. 2(b)]. By grouping 12 neighboring sites into a new supersite (Fig. 3), the original system with further-neighbor couplings is transformed into a thermodynamically equivalent system in which all important couplings are nearest-neighbor between supersites. The symmetries of the eight ground states (empty, 2×2 solid which is fourfold degenerate, and $\sqrt{3} \times \sqrt{3}$ solid which is threefold degenerate) are preserved, and each ground state corresponds to a ferromagnetic alignment of the variables at the supersites; i.e., each ground state has the same translational symmetry as the lattice of supersites. This prefacing transformation is made quantitative by a partial trace of the original partition function, which is carried out approximately. The resulting system can be seen as composed of coupled[25] three- and four-state Potts[26] spins, and thermodynamic (annealed) vacancies.[2] Two characteristics of the new model, that all essential couplings are nearest-neighbor and that all corresponding orderings are ferromagnetic, make it particularly amenable to an approximate, Migdal-Kadanoff-type renormalization calculation.[27,28] The corresponding renormalization trajectories are in a space of seven thermodynamic fields.

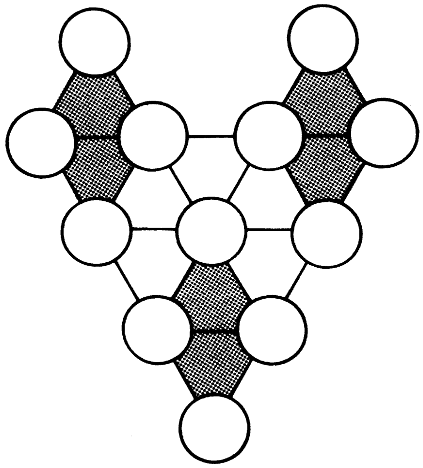

FIG. 3. Group of 12 lattice-gas sites, underlying a single supersite in the prefacing transformation.

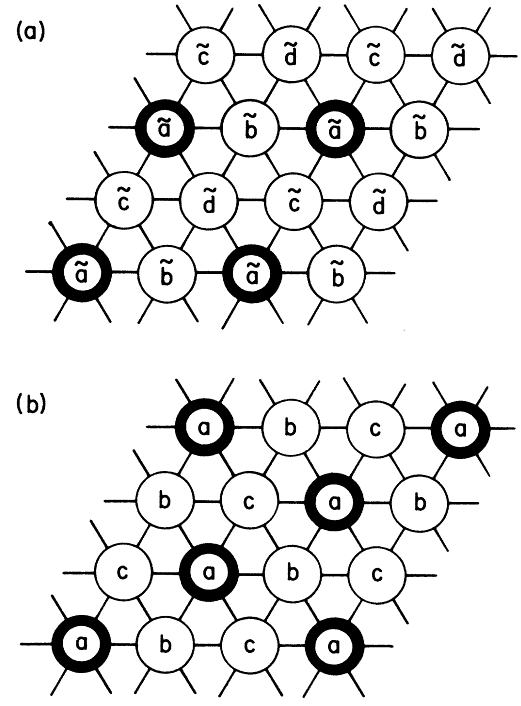

FIG. 2. (a) The triangular lattice can be decomposed into four equivalent sublattices. The dark circles represent the occupied sites of a perfect 2×2 solid. (b) The triangular lattice can also be decomposed into three equivalent sublattices, leading to a $\sqrt{3} \times \sqrt{3}$ solid.

A variety of phase diagrams is obtained, as the diameter σ of the Lennard-Jones potential which determines the lattice-gas interactions is scanned from 1.4 to $1.9a$, where a is the lattice constant of the adsorption sites ($a = 2.46$ Å in basal graphite). The method is quite generally applicable. Thus, a somewhat different sequence of phase diagrams is obtained for a lattice gas with nearest-neighbor exclusion and second,- third-, fourth-neighbor interactions only. These phase diagrams variously exhibit first-order structural transitions between the two solids, first- or higher-order melting transitions between one solid and a fluid, and first-order liquid-gas transitions. Multicritical points, critical end-points, and liquid-gas critical points are encountered. A bicritical topology is approached as the limit of the latter phase diagram sequence. We also report a solid-liquid-gas triple point, which, to our knowledge, has not been obtained in any previous renormalization theory. In certain phase diagrams, the 2×2 solid occurs at finite temperature, but not at zero temperature.

Recent x-ray-scattering results[29] indicate that the commensurate solids of xenon submonolayers on graphite are preempted by an incommensurate solid. Since we cover a rather large range of potentials, our results could be useful to other experiments, either in physisorption, or in chemisorption. For systems such as physisorbed xenon which exhibit incommensurate phases not taken into account here, our phase diagrams can be considered the outer limit for commensurate ordering. We make contact with the phase diagram of methane physisorbed on graphite, as deduced from neutron scattering, which has both commensurate and incommensurate solids,[30] as well as distinct liquid and gas phases in coexistence.[31] This leads to the suggestion that the effective hard-core radius of methane is increased by adsorption. In chemisorbed systems, on the other hand, ordered phases are commensurate, and structural transitions between such phases have been reported from low-energy electron diffraction (LEED) experiments.[32,33] Specifically, we obtain a phase diagram very similar to that measured[33] for oxygen on nickel (111), with both 2×2 and $\sqrt{3}\times\sqrt{3}$ structures.

The structural phase transitions obtained here are difficult to study by computer experiments. Since the two solid phases have lattice constants of $2a$ and $\sqrt{3}a$, the transition requires a rearrangement of an entire domain. Thus, in Monte Carlo simulations we have performed, severe metastability problems were encountered.

II. METHOD

Figure 1 shows the triangular array of preferred adsorption sites on the basal surface of graphite. Each site is either empty or occupied by a single adatom. The exact form of the interaction between adatoms is not well known. In physisorption, it can be presumed that this interaction is not much different than in a three-dimensional gas, since the van der Waals force causing adsorption is too weak to affect much the internal electronic structure of an adatom. Thus, previous experimental data on noble gases has been analyzed in terms of a Lennard-Jones pair potential,

$$V(r)=4\epsilon[(\sigma/r)^{12}-(\sigma/r)^{6}] \quad , \tag{1}$$

yielding a diameter σ indistinguishable from three dimensions, and a well depth ϵ about 20% shallower than in three dimensions.[6,19] Accordingly, our main reported results are for a lattice gas with Hamiltonian

$$\mathcal{H}(n)=\sum_m J_m \sum_{\langle ij\rangle_m} n_i n_j-\mu\sum_i n_i \quad , \tag{2}$$

where $n_i=0(1)$ when site i is empty (occupied), $\langle ij\rangle_m$ indicates summation over mth-neighbor pairs of sites, and μ is the chemical potential. A Lennard-Jones potential [Eq. (1)] determines the potential energies J_m of two adatoms at mth-neighbor sites $\langle ij\rangle_m$,

$$J_m=V(|\vec{r}_i-\vec{r}_j|) \quad , \tag{3}$$

where $\vec{r}_i$ is the position of site i. We study a sequence of systems by varying σ from 1.4 to $1.9a$, where a is the nearest-neighbor separation. This range of σ values gives systems with effective nearest-neighbor exclusion and favorable further-neighbor interactions, which is appropriate for adsorbates on graphite with hard cores comparable to or larger than that of krypton. The nearest-neighbor exclusion is not essential to our method, but simplifies the computation, as seen below. In fact, our approach is applicable to general further-neighbor pair interactions, without the restriction of Eq. (3), and to triplet and other many-particle interactions. Thus, we also report results for a sequence of systems obtained by varying J_3/J_2, with J_1 positive infinite (hard-core exclusion), J_4 equal to $0.3J_2$, and all other J_m equal to zero. These systems, being more accessible to Monte Carlo simulation,[34] could provide the possibility of direct comparison between the two methods. Furthermore, we discover that, by changing the parametrization of further-neighbor interactions, new types of phase diagrams are encountered.

As mentioned in the previous section, we expect to derive the ordered arrangements of the $\sqrt{3}\times\sqrt{3}$ and 2×2 commensurate solids, depicted in Figs. 2. By symmetry, a transition from a disordered lattice gas to these ordered phases should be[15,16] in the universality classes of the two-dimensional three- and four-state Potts models,[26] respectively. Classical mean-field theory fails qualitatively by predicting first-order phase transitions for these Potts models, contrary to rigorous results.[35] On the other hand, renormalization theory has been successful in this regard.[36] It is rather difficult, however, to carry out a renormalization calculation directly on the systems given by Eq. (2), because of the further-neighbor interactions and the antiferromagnetic ordered states. Therefore, a prefacing transformation is used.[2]

Consider the group of 12 lattice-gas sites shown in Fig. 3. The four sites of a diamond are a unit cell of the 2×2 solid. Three such diamonds are taken together, to accomodate the structure of the $\sqrt{3}\times\sqrt{3}$ solid. From this group of 12 sites, a single local unit is constructed, and called a supersite. This is the basis of the prefacing transformation. The sites throughout the entire lattice gas are separated into groups of 12, and each group becomes a single supersite. The supersites form a triangular lattice. Both the 2×2 and $\sqrt{3}\times\sqrt{3}$ solids have ferromagnetic representations in the supersite system.

In terms of lattice-gas states (each site empty or occupied), each group of 12 sites has 2^{12} configurations, but nearest-neighbor exclusion allows only 134 of these to occur. Eight states are distinguished for each supersite, and labeled with the occupation variables t and $\tilde{t}$, and with the Potts variables s and $\tilde{s}$. These are the states of empty ($t=\tilde{t}=0$), preferentially occupied in one of the four sublattices of the 2×2 solid ($t=0$, $\tilde{t}=1$, and $\tilde{s}=\tilde{a}$, $\tilde{b}$, $\tilde{c}$, or $\tilde{d}$), or preferentially occupied in one of the three sublattices of the $\sqrt{3}\times\sqrt{3}$ solid ($\tilde{t}=0$, $t=1$, and $s=a$, b, or c). These eight structures can be discerned in the 134 lattice-gas configurations. Thereby, each lattice-gas configuration is associated with supersite states, essentially by a majority rule.[24] This is made precise with a projection operator, $P(t,s,\tilde{t},\tilde{s};\{n_1,n_2,\ldots,n_{12}\})$, which is nonzero if the arguments satisfy the association.

The assignment of the 134 lattice-gas configurations to the eight supersite states is done by a double majority rule.[37] For each lattice-gas configuration, first a choice is made between the empty or occupied supersite states, then a choice is made between the various alignments of the occupied state. Note that 5 is the maximum number of adatoms in the group of 12 sites. A configuration having zero or one adatom is assigned to the empty supersite state. A configuration having two or more adatoms is assigned to the occupied ($t+\tilde{t}=1$) supersite states. Among the seven occupied supersite states, a majority rule[24] is used. The configuration is assigned to the state with the largest occupation in the corresponding sublattice. When there is a tie between a 2×2 and a $\sqrt{3}\times\sqrt{3}$ sublattice, assignment is to the 2×2 state, because a smaller number of adatoms is necessary to accomplish the 2×2 structure. When there is a tie between sublattices of the same structure, the configuration is shared among the corresponding states. The projection operator has the value of 1/(number of recipient supersite states).

The Hamiltonian of the supersite system is determined by a partial sum of the partition function of the lattice gas, using the projection operator:

$$e^{-\mathcal{H}(t,s,\tilde{t},\tilde{s})/kT}=\sum_{\{n\}}\left[\prod_{i'}P_{i'}(t,s,\tilde{t},\tilde{s};\{n\})\right]e^{-\mathcal{H}(n)/kT}\ , \tag{4}$$

where the product is over all supersites. The partition function is conserved under this prefacing transformation,

$$Z=\sum_{\{n\}}e^{-\mathcal{H}(n)/kT}=\sum_{\{t,s,\tilde{t},\tilde{s}\}}e^{-\mathcal{H}(t,s,\tilde{t},\tilde{s},)/kT}\ . \tag{5}$$

Unfortunately, Eq. (4) cannot be performed exactly. We therefore resort to a two-cell approximation.[24] A quasiperiodic boundary condition is used, realized by surrounding each cell with six replicas of the other,[37]

$$\exp(-6\mathcal{H}_{i'j'}/kT)=\sum_{\{n\}_{i'},\{n\}_{j'}}P_{i'}P_{j'}\exp\left[-\sum_{\hat{r}}^{6}\mathcal{H}_{\hat{r}}(\{n\}_{i'},\{n\}_{j'})/kT\right]\ , \tag{6}$$

where the $\hat{r}$ sum is over the six possible lattice directions between the nearest-neighbor supersites i' and j'. The supersite Hamiltonian $\mathcal{H}_{i'j'}$ from Eq. (6) is translationally averaged, i.e., averaged over the 12 distinct ways of constructing supersites from the original lattice gas. [The quasiperiodic boundary condition in Eq. (6) is equivalent to rotational averaging.] A nearest-neighbor supersite Hamiltonian results,

$$\mathcal{H}(t,s,\tilde{t},\tilde{s})=\sum_{\langle i'j'\rangle_1}\mathcal{H}_{i'j'}\ , \tag{7a}$$

$$-\mathcal{H}_{i'j'}/kT=(K_1\delta_{s_{i'},s_{j'}}+K_2)t_{i'}t_{j'}+K_3(t_{i'}+t_{j'})+(K_4\delta_{\tilde{s}_{i'},\tilde{s}_{j'}}+K_5)\tilde{t}_{i'}\tilde{t}_{j'}+K_6(\tilde{t}_{i'}+\tilde{t}_{j'})+K_7(t_{i'}\tilde{t}_{j'}+\tilde{t}_{i'}t_{j'})+K_8\ , \tag{7b}$$

where i' labels supersites, $\langle i'j'\rangle_1$ indicates summation over pairs of nearest-neighbor supersites, $\delta_{s_{i'},s_{j'}}=1(0)$ for $s_{i'}=s_{j'}(s_{i'}\neq s_{j'})$, and the interaction constants K_u are functions of the lattice-gas parameters,

$$K_u=K_u(\{J_m/kT\},\mu/kT)\ . \tag{8}$$

The first two terms in Eq. (7b) describe a three-state Potts model with thermodynamic vacancies,[2] also called a three-state Potts lattice gas (P_3LG). The next two terms describe a four-state Potts lattice gas (P_4LG). The fifth term couples P_3LG and P_4LG. The last term is an additive constant. This completes the prefacing transformation.

The statistical mechanics of the supersite problem is done by a renormalization method.[23,24] A Migdal-

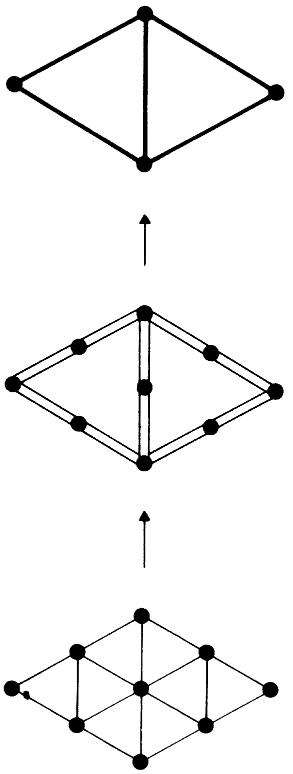

FIG. 4. Migdal-Kadanoff transformation for the triangular lattice. The length rescaling factor here is $b=2$.

Kadanoff-type[27,28] bond-moving approximation for the triangular lattice (Fig. 4) is used, which is described elsewhere.[2] Renormalization trajectories are in the seven-dimensional space of $\{K_1, K_2, \ldots, K_7\}$. The techniques for obtaining global phase diagrams are detailed elsewhere.[37] The new aspect here is that the first performed transformation is prefacing (restructuring), instead of renormalization (rescaling). It may be worthwhile to exhibit one relation of this first transformation. Let ψ_m and ϕ_u be the densities conjugate to J_m and K_u, respectively, in the lattice-gas and supersite systems:

$$\psi_m = -\frac{kT}{N}\frac{\partial}{\partial J_m}\ln Z \ , \qquad \phi_u = \frac{12}{N}\frac{\partial}{\partial K_u}\ln Z \ , \tag{9}$$

where N is the number of lattice-gas sites, and therefore $\frac{1}{12}N$ is the number of supersites after prefacing. Let us define $J_0 \equiv \mu$, the chemical potential, so that $\psi_0 \equiv n$ is the coverage, i.e., the number of adatoms per adsorption site. From the chain rule,

$$\psi_m = -\tfrac{1}{12}kT\sum_{u=1}^{8}\phi_u\frac{\partial K_u}{\partial J_m} \ , \tag{10}$$

which is used in the calculation of densities.

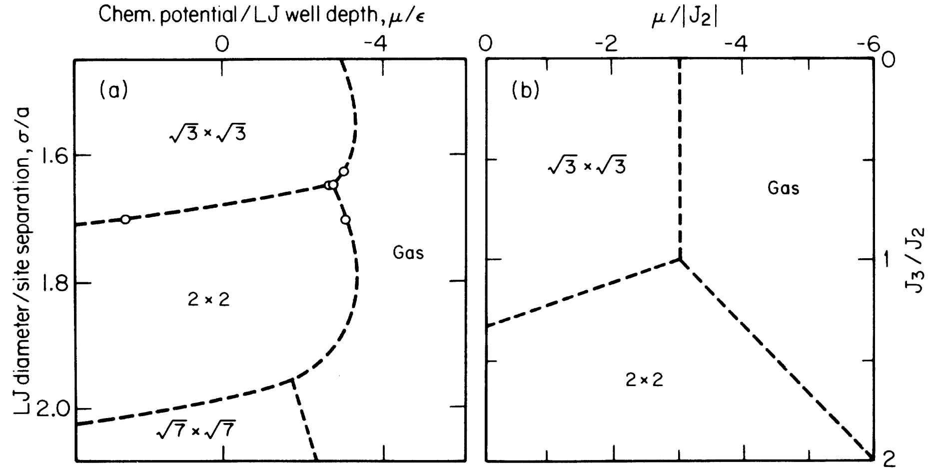

FIG. 5. Exact zero-temperature phase diagrams, the dashed lines indicating first-order phase transitions. (a) The Lennard-Jones lattice gas. The zero-temperature intercepts of Figs. 6(a),6(i),6(k) are shown by the circles. This diagram is reproduced by our calculation, indistinguishably on this figure. (b) The $(J_2, J_3, J_4 = 0.3J_2)$ lattice gas. This diagram is reproduced exactly by our calculation.

III. RESULTS

A. Global phase diagrams

Our method yields phase diagrams for a variety of interatomic potentials. This is demonstrated here with two specific sequences. One sequence is of a Lennard-Jones lattice gas, as defined by Eqs. (1)–(3). In this case, up to 20th-neighbor couplings participate in our approximate prefacing transformation. The sequence is obtained by changing σ/a, the ratio of adatom diameter to site separation, from 1.4 to 1.9. The other sequence is of a lattice gas with nearest-neighbor exclusion and only J_2, J_3, and $J_4 = 0.3J_2$ nonzero. The ratio J_3/J_2 is varied between 0.3 and infinity, so that the 2×2 structure goes from being less favored to being heavily favored by the interactions. We shall refer to this sequence as the $(J_2, J_3, J_4 = 0.3J_2)$ lattice gas. The global phase diagrams occur in the space of temperature $(kT/\epsilon, kT/J_2)$, chemical potential $(\mu/\epsilon, \mu/J_2)$ or fraction of sites occupied (coverage n), and potential range $(\sigma/a, J_3/J_2)$.

Exact zero-temperature phase diagrams are easily obtained by ground-state analysis. They are shown in Figs. 5. Our prefacing-renormalization procedure reproduces the exact zero-temperature phase diagram of the $(J_2, J_3, J_4 = 0.3J_2)$ lattice gas, because the prefacing transformation takes into account all of the interactions entering the ground states, and the Migdal-Kadanoff renormalization transformation becomes self-consistent in the strong coupling limit.[27,28,38] Our procedure reproduces very accurately the zero-temperature phase diagram of the Lennard-Jones lattice gas. For example, the zero-temperature intercepts of Figs. 6(a),6(i),6(k) are shown as data points in Fig. 5(a). Thus, in this figure, our calculation is indistinguishable from the exact curve. This is because the prefacing transformation takes into account all important interactions. At infinite temperature, the problem reduces to the hard-hexagon system, and we obtain a second-order transition at density $n = 0.283$ and chemical potential $\mu/kT = 2.59$, to be compared to previous best estimates[39] of n between 0.275 and 0.280 and μ/kT between 2.39 and 2.42. This also suggests that our chosen projection operator in prefacing is a sensible one, since this error in chemical potential is comparable in magnitude to and in the same direction as the errors for K_u^* from the renormalization-group calculation (Table I).

Finite-temperature phase diagrams are obtained as cross sections of the global phase diagram at constant interaction potential. At finite temperatures, commensurate domains deviate from their ideal coverage values, $n = \frac{1}{4}$ and $\frac{1}{3}$ for 2×2 and $\sqrt{3}\times\sqrt{3}$, by accommodating vacancies.[40(a)] These phase diagrams are displayed in Figs. 6 and 7 (temperature versus chemical potential on the left side and correspondingly temperature versus coverage on the right side), and discussed below, including their relation to experimental results for methane on graphite and oxygen on nickel.

B. Lennard-Jones lattice gas

(i) Figures 6(a) and 6(b) for $\sigma/a = 1.6300$. The phases which appear are the $\sqrt{3}\times\sqrt{3}$ solid and a two-dimensional fluid, the latter having equivalent occupation of all sublattices. This type of phase diagram is encountered down to $\sigma/a = 1.4$. The phase diagrams here and in Sec. III B (*ii*) below have the topology exhibited by krypton ($\sigma/a \simeq 1.46$) and nitrogen ($\sigma/a \simeq 1.50$) adsorbed on basal graphite.[9,10,2,3] The solid and the fluid are separated by first-order phase transitions at low temperatures, which is seen as a boundary line in the temperature versus chemical potential diagram, and as a coexistence region in the temperature versus coverage diagram. The $\sqrt{3}\times\sqrt{3}$ solid and the fluid are separated by a line of higher-order (continuous) phase transitions at high temperatures. The higher- and first-order transitions meet at the multicritical point M_4. In the region marked as $\sqrt{3}\times\sqrt{3}$, actually 3 degenerate, but distinct $\sqrt{3}\times\sqrt{3}$ solids coexist, each corresponding to the preferential occupation of one of the three sublattices *a*, *b*, and *c*. These become critical at the higher-order line, which is therefore a line of tricritical points. The three $\sqrt{3}\times\sqrt{3}$ solids obey a threefold permutation symmetry,[15] and, indeed, the higher-order line renormalizes onto an explicitly three-state Potts fixed-point Hamiltonian. The three $\sqrt{3}\times\sqrt{3}$ solids and the fluid coexist along the first-order boundary in Fig. 6(a), and, equivalently, within the coexistence region in Fig. 6(b). These four phases achieve criticality at the multicritical point M_4, which can therefore be called a fourth-order point. This point is further discussed below. As σ/a is increased, this type of phase diagram is still encountered, but a large segment of the boundary between the fluid and the coexistence region becomes very flat, i.e., occurs at nearly constant temperature.[9,10,3]

(ii) Figures 6(c) and 6(d) for $\sigma/a = 1.6455$. These two phase diagrams are topologically equivalent to the previous two, but two important differences should be noted. First, new structure occurs in the coexistence boundary. As seen from Fig. 6(d), the coexistence region is composed of a large low-temperature portion terminating at the flat boundary with the fluid, and of a smaller narrower cap terminating at the multicritical point M_4'. In terms of renormalization theory, these two portions are the domains of attraction of two separate first-order fixed points. In between passes the domain F_4 of another, unstable first-order fixed point, which, when σ/a is further increased, splits into a solid-liquid-gas triple point and a liquid-gas critical point. Second, the multicritical point M_4' renormalizes to a different fixed point than

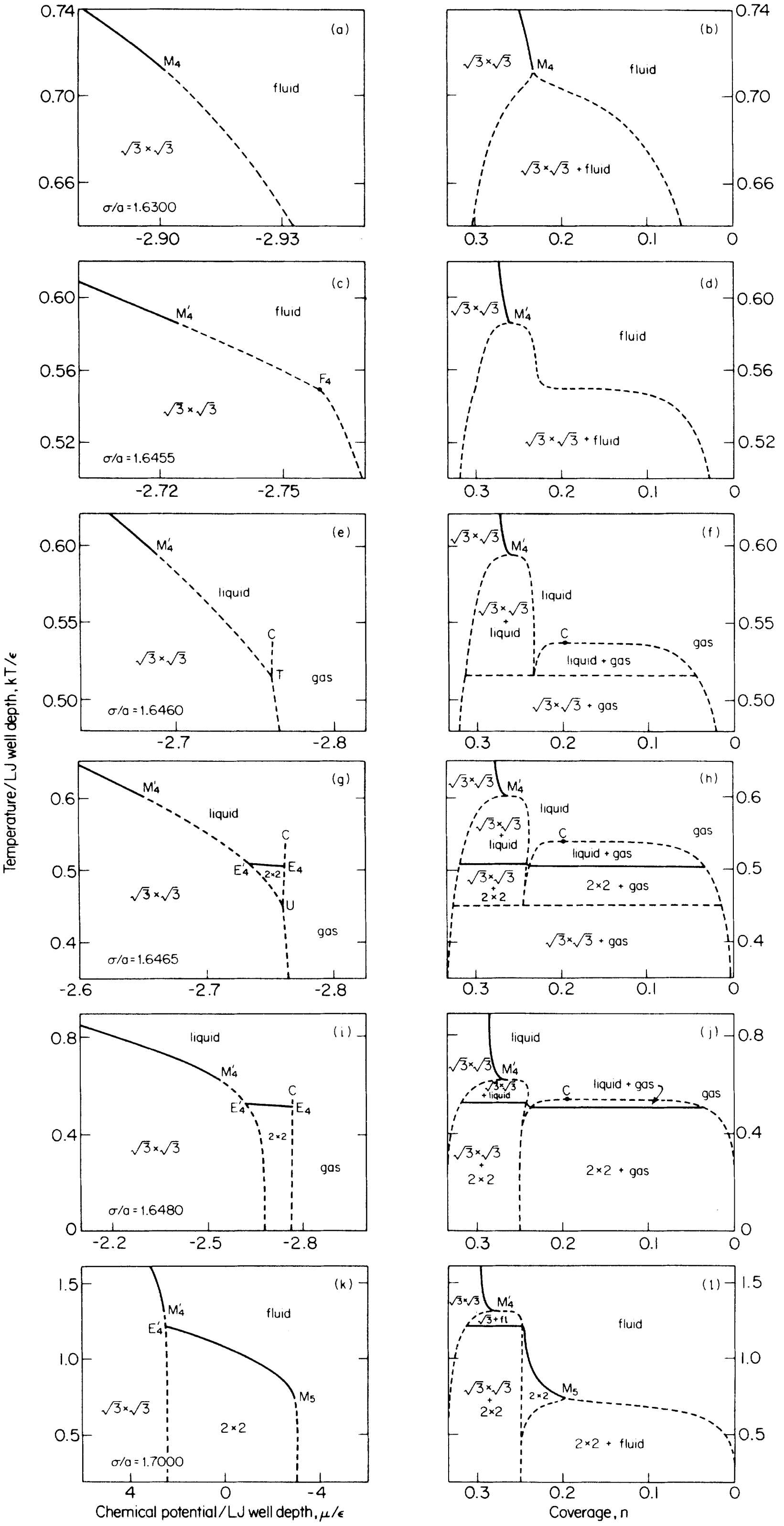

FIG. 6. Calculated phase diagrams of the Lennard-Jones lattice gas. First- and higher-order phase transitions are indicated by dashed and full lines, respectively.

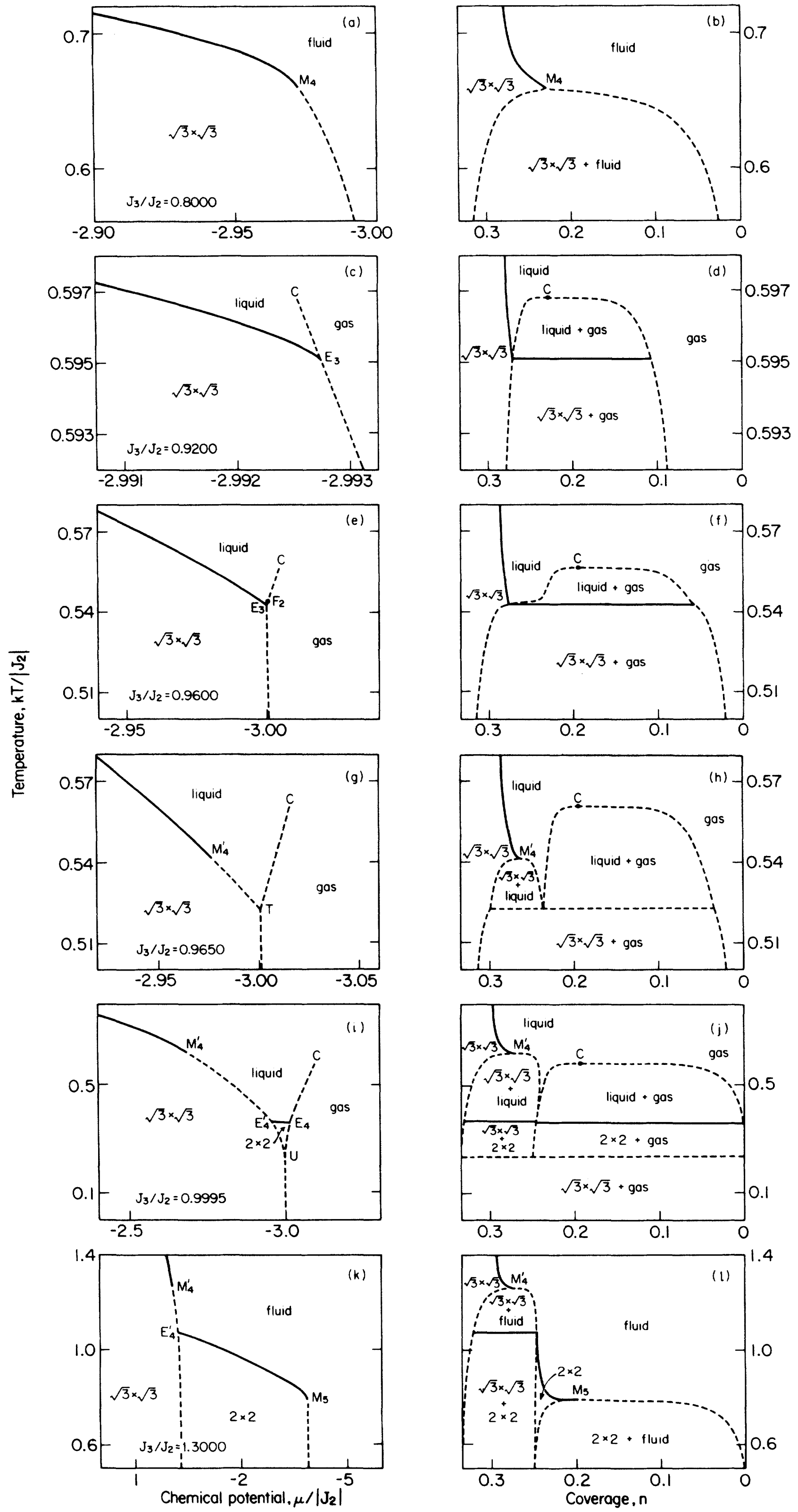

FIG. 7. Calculated phase diagrams of the ($J_2,J_3,J_4=0.3J_2$) lattice gas. First- and higher-order phase transitions are indicated by dashed and full lines, respectively.

M_4 above, and, within our approximation, M_4' and M_4 appear to be in different universality classes. For example, the coexistence boundary is cusped at M_4, but rounded at M_4'. Equivalently (Sec. III D), in the temperature versus coverage diagrams, the higher-order line reaches M_4 with finite slope, but M_4' with zero slope. The universality class of a multicritical point should be determined by the comparative properties of the phases whose coexistence terminates at the multicritical point. Indeed, the coexistence regions below M_4 and M_4' are different. The coexistence region terminating at M_4 renormalizes to the same fixed point as the low-temperature portion of the coexistence region in Fig. 6(d). The difference between M_4 and M_4' is further pursued in Sec. III D below.

(iii) Figures 6(e) and 6(f) for $\sigma/a = 1.6460$. By the mechanism mentioned above, the liquid-gas critical point C and the solid-liquid-gas triple point T have appeared. Like the fluid in the previous phase diagrams, the liquid and the gas have no preferential sublattice occupation. They differ from each other with respect to density.[2] For example, within the liquid-gas coexistence region, two types of domain coexist, one dense and the other dilute. These phase diagrams have the topology of phase diagrams commonly exhibited by three-dimensional materials, except that the melting transition becomes higher order at high temperatures. The multicritical point is still M_4', which will persist in all subsequent phase diagrams we present for the Lennard-Jones lattice gas. The liquid valley at coverage $n \simeq \frac{1}{4}$ can be interpreted as a melted 2×2 solid, and is a precursor to the appearance of this solid.

(iv) Figures 6(g) and 6(h) for $\sigma/a = 1.6465$. At this value of the Lennard-Jones diameter, the third-neighbor interaction is sufficiently strong to produce a 2×2 solid phase, first appearing at finite temperature in the region which was the liquid above to the triple point in the previous phase diagram. In this phase diagram, the 2×2 solid terminates at low temperature at the eutectic point U of $\sqrt{3}\times\sqrt{3}$ solid-2×2 solid-gas coexistence. The 2×2 solid is separated by first-order phase transitions from the $\sqrt{3}\times\sqrt{3}$ solid and from the gas. It is separated from the liquid by a line of higher-order phase transitions. Within the 2×2 region, 4 degenerate, but distinct solids coexist, each preferentially occupying one of the four sublattices $\tilde{a}$, $\tilde{b}$, $\tilde{c}$, or $\tilde{d}$. These obey a fourfold permutation symmetry.[16] The higher-order transition line renormalizes onto a four-state Potts fixed-point Hamiltonian. This line is preempted by first-order transitions at the critical end-points E_4' and E_4. Among the variety of constant coverage scans featured in Fig. 6(h), one at the fixed coverage of $n \lesssim \frac{1}{4}$ shows, as temperature is lowered, the coexistence of $\sqrt{3}\times\sqrt{3}$ solid and liquid, followed (after narrow temperature intervals of single liquid and single 2×2) by the coexistence of 2×2 solid and gas, followed by the coexistence of $\sqrt{3}\times\sqrt{3}$ solid and gas. The variety of distinct regions in Fig. 6(h) is reminiscent of intercalation systems.[40(b)] The relation of Fig. 6(h) to methane physisorbed on graphite is discussed in Sec. III E below.

(v) Figures 6(i) and 6(j) for $\sigma/a = 1.6800$. The eutectic point has moved to zero temperature and has disappeared. The 2×2 solid reaches zero temperature.

(vi) Figures 6(k) and 6(l) for $\sigma/a = 1.7000$. The critical end-point E_4 has moved to the tip of the coexistence region and merged with C, resulting in the multicritical point M_5. The liquid-gas transition has disappeared. The multicritical point M_5 is a fifth-order phase transition point, since it terminates a coexistence of the four 2×2 solids and the fluid. The 2×2 solid deviates from its ideal coverage $\frac{1}{4}$, on the dilute side, by accomodating vacancies. On the dense side, rather than accomodating interstitials, it breaks up into domains in coexistence with the $\sqrt{3}\times\sqrt{3}$ solid.[40] The relation of Fig. 6(l) to oxygen chemisorbed on nickel is discussed in Sec. III E below.

When $\sigma/a \simeq 1.96$, a $\sqrt{7}\times\sqrt{7}$ solid appears at zero temperature [Fig. 5(a)]. Since this type of ordering is not projected in our prefacing transformation, the present treatment does not apply for $\sigma/a \gtrsim 1.9$.

C. $(J_2, J_3, J_4 = 0.3J_2)$ lattice gas

This sequence of systems is obtained by varying J_3/J_2, with J_1 positive infinite (hard-core exclusion) and $J_2, J_3, J_4 = 0.3J_2$ negative (favorable). Fifth- and further-neighbor interactions were set to zero. These systems are more accessible to Monte Carlo simulation,[34] and it is hoped that direct comparison between the two methods can be achieved. (However, Monte Carlo simulations which we have performed have had severe problems of hysteresis in the structural phase transition between the $\sqrt{3}\times\sqrt{3}$ and 2×2 solids, since the entire lattice must rearrange.)

Our quantitative results are given in Figs. 7. The qualitative difference between the Lennard-Jones lattice gas and the $(J_2, J_3, J_4 = 0.3J_2)$ lattice gas is seen in the phase diagrams between Figs. 6(b) and 6(g), on the one hand, and Figs. 7(b) and 7(i), on the other hand. In the Lennard-Jones case, as the range of interaction (σ/a) is increased, the multicritical point M_4 splits into the multicritical point M_4' and the unstable first-order point F_4. At that stage, a narrow cap occurs on the high coverage side of the solid-fluid coexistence region. Upon further increase of the interaction range, a liquid-gas coexistence region is started at the low coverage side of the cap, when F_4 splits into the triple point T and the critical point C. In the $(J_2, J_3, J_4 = 0.3J_2)$ case, again as the range of interaction (J_3/J_2) is increased, the multicritical point M_4 splits into a liquid-gas critical point $C_{(3)}$ and a critical end-point E_3. Then, $C_{(3)}$ splits into another liquid-gas critical point $C_{(4)}$ and an unstable first-order point F_2. In this case, the liquid-gas coexistence region has a narrower cap on the low coverage side and a broader base at lower temperatures, separated by F_2, and each flowing to its own first-order fixed point. The underlying mechanism is that our system reduces to an ordinary lattice gas in two ways, namely either via $\mathrm{P_3LG}$ with K_2 of Eq. (7b) dominant, or via $\mathrm{P_4LG}$ with K_5 dominant. Nevertheless, the corresponding fixed points $C^*_{(3)}$ and $C^*_{(4)}$ are algebraically equivalent and both in the Ising[41] universality class. The small (0.1% and 1.0%) difference between their exponents given in Table I is due only to the approximate nature of our renormalization. Accordingly, the liquid-gas critical points are denoted in Figs. 6 and 7 without the superfluous subscript.[42] As J_3/J_2 is further increased, a solid-liquid coexistence region is started at the high coverage side of the cap, when F_2 and E_3 come together and separate off as the multicritical point M_4' and the triple point T.

It should be recalled that the Lennard-Jones lattice gas and the $(J_2, J_3, J_4=0.3J_2)$ lattice gas determine two different sequences of two-dimensional surfaces (Figs. 6 and 7) within the seven-dimensional phase diagram of the coupled Potts models [Eq. (7)] to which renormalization is applied. The special points of Figs. 6 and 7 actually occur as five-dimensional hypersurfaces. These meet at four-dimensional hypersurfaces, which include points isolated between the phase diagrams of Figs. 6 and 7 (e.g., the isolated point where M_4 splits into E_3 and C), and occurring differently in the two sequences. The effect of one such isolated point is seen in Fig. 7(l). The multicritical points M_5 in Figs. 6(k), 6(l) and 7(k), 7(l) renormalize to the same fixed points M_5^* (see Table I) and, thus, have the same critical exponents. Specifically, as reflected in the exponent $\beta_{24}=1.29$ being greater than one, the coexistence boundary should not be flat at M_5 and the higher-order line should reach M_5 with nonzero slope (Sec. III D). Whereas these expectations are satisfied in Fig. 6(l), they seem violated in Fig. 7(l). The reason is that the $J_3/J_2=1.3$ value is very close to that of the isolated point occurring between Figs. 7(i), 7(j) and 7(k), 7(l), where E_4 and C merge into M_5. The renormalization trajectory originating at M_5 in Figs. 7(k), 7(l) flows very close to, and, therefore, undergoes many iterations near the triply unstable fixed point of this isolated point, before continuing on to M_5^*. The coexistence boundary exponent of the triply unstable fixed point is $\beta_{24}=0.15$, which is less than one, meaning a flat boundary and a zero slope of the higher-order line. Thus, Fig. 7(l) exhibits a crossover phenomenon, by depicting the effects of the close proximity of another universality class at $J_3/J_2 \lesssim 1.3$.

The topology of Figs. 7(k), 7(l) persists to all higher J_3/J_2 values. Figures 8 show the limit of this sequence, $J_3/J_2=\infty$, which is equivalent to a lattice gas with $J_1=\infty$, $J_3<0$, and all other interactions zero. The higher-order of 2×2 ordering has developed a maximum. The end-point E_4' (terminating the higher-order line of 2×2 ordering) and the multicritical point M_4' (terminating the higher-order line of $\sqrt{3}\times\sqrt{3}$ ordering) have considerably approached each other, but have not merged into a bicritical point.[43] On the scale dictated by the temperatures at which these special points occur, the phase diagram would effectively exhibit a bicritical topology, but the blowup in Fig. 8(a) reveals the true structure. This is very similar to the effective, but not true, tricritical phase diagram obtained[44] for the two-dimensional XY model, again using the Migdal-Kadanoff procedure. The further inclusion of unfavorable second-neighbor interaction does not qualitatively change the picture of Figs. 8.

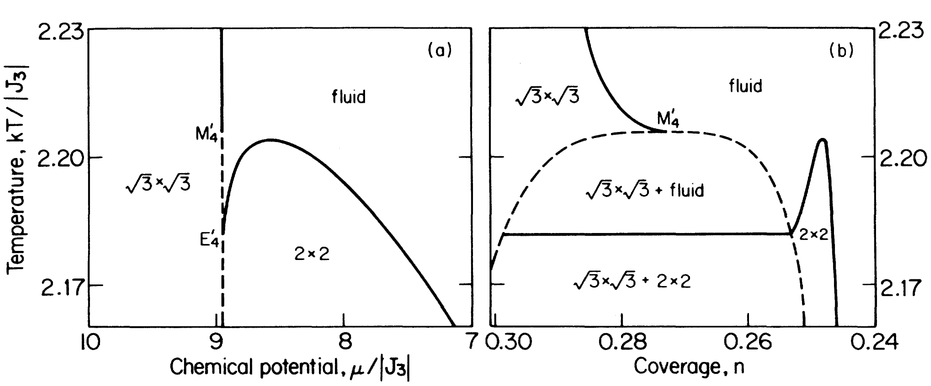

FIG. 8. Detail of the phase diagram for a lattice gas with $J_1=\infty$, $J_3<0$, and all other J_m zero. This is equivalent to $J_3/J_2=\infty$, the limit of the sequence of Fig. 7. The regions of the phase diagram not shown here are qualitatively as in Figs. 7(k), 7(l).

TABLE I. Fixed points and their relevant eigenvalue exponents. We have not listed less stable versions of these fixed points, which are due only to redundant eigenvalues and which have the very same physical eigenvalues as given here.

Fixed point	Type	Eigenvalue exponents (rigorous or conjectured)		Location (rigorous)						
		y_2	y_4	K_1^*	K_2^*	K_3^*	K_4^*	K_5^*	K_6^*	K_7^*
$C_{(3)}^*$	Ising	1.8746 (1.875)[a]	0.77 (1)[a]	0	1.262 (1.099)[a]	$-K_2^*/2-0.173$ $(-K_2^*/2-0.183)$	0	K_2^*	$-\infty$	K_2^*
$C_{(4)}^*$	Ising	1.8723 (1.875)[a]	0.78 (1)[a]	0	K_5^*	$-\infty$	0	1.287 (1.099)[a]	$-K_5^*/2-0.219$ $(-K_5^*/2-0.231)$	K_5^*
P_3^*	3-Potts		0.83 (1.2)[b]	0.693 (0.630)[c]	−0.29	∞	0	0	$-\infty$	0
E_3^*	End-point	2 (2)	0.83 (1.2)	0.693 (0.630)	∞	$-K_2^*/2-0.37$	0	0	$-\infty$	$-0.33, \infty$
M_4^*	Multicritical	1.489 (1.5?)	0.23 (0?)	1.29	−0.58	−0.26	0	0	$-\infty$	0
$M_4'^*$	Multicritical	1.788 (1.714)[d]	0.64	1.66	−0.47	∞	0	0	$K_3^*+0.36$	0
P_4^*	4-Potts		0.89 (1.5)[e]	0	0	$-\infty$	0.756 (0.693)[c]	−0.25	∞	0
E_4^*	End-point	2 (2)	0.89 (1.5)	0	0	$-\infty$	0.756 (0.693)	∞	$-K_5^*/2-0.40$	$-0.42, \infty$
$E_4'^*$	End-point	2 (2)	0.89 (1.5)	∞	$\pm\infty$[f]	$\pm\infty$[f]	0.756 (0.693)	−0.25	$[K_1^*+K_2^*]/2+K_3^*-0.28$	$-\infty$[f]
M_5^*	Multicritical	1.406 (1.5)[d]	0.46 (0)[d]	0	0	$-\infty$	1.06	−0.37	−0.21	0

[a] Reference 41, rigorous.

[b] Reference 47, conjectured.

[c] Reference 46, rigorous.

[d] Reference 36, conjectured.

[e] Reference 45, rigorous.

[f] At $E_4'^*$, the following inequalities are obtained: $1 \ll K_1^*+K_2^*, K_1^*+2K_2^*+2K_3^*, K_2^*-2K_7^*, 2K_6^*+K_7^*$.

D. Critical exponents

The fixed-point locations and relevant (i.e., positive) eigenvalue exponents for the higher-order transitions are given in Table I. Comparison with rigorous[41,45,46] or conjectured[47,36] exact values, given in parentheses, shows that the smallest relevant exponenets y_4 have errors ranging from -22% to -41%. The leading exponents y_2, on the other hand, are remarkably accurate. This accuracy trend has been noted[37,2] in position-space renormalization treatments of two-dimensional systems. The exponents y_2 correspond to singularities observed upon approaching the phase transition from a direction which is not parallel to the phase coexistence direction. The fixed points of first-order transitions have an exponent equal[48] to the dimensionality, $y_2 = 2$. The fixed points of the triple point T and the eutectic point U have two such exponents equal to the dimensionality. The fixed points of the end-points[37] have the exponent y_4 exactly equal to that of the transition line which is terminated, so that no new singularity is introduced. They also have another unstable direction, with $y_2 = 2$, characteristic of first-order transitions.

We had mentioned the occurrence of two types of multicritical points, M_4 and M_4', terminating the higher-order phase transitions between the $\sqrt{3} \times \sqrt{3}$ solid and the fluid. It could well be that this differentiation is an artifact of our approximate renormalization procedure. This would be suggested by general consideration of the topology of the phase diagram and the symmetry of the phases. Nevertheless, the contrast between M_4 and M_4' is intriguing, and we would like to pursue it somewhat further. The exponents y_2 of M_4 and M_4' differ by an amount significantly larger than our error for such leading exponents, estimated from comparison with the exact values given in parentheses in Table I. Both M_4 and M_4' terminate the coexistence of three degenerate solids and one fluid. However, at least with respect to density, the coexistence region below M_4 comes within a few precent of achieving a fourfold symmetry.[2] For example, M_4 occurs at coverages very close to $\frac{3}{4}$ of a perfect $\sqrt{3} \times \sqrt{3}$ monolayer, whereas M_4' occurs at higher coverages.

If a $(q=3)$-state Potts transition, which is the type of the transition between the $\sqrt{3} \times \sqrt{3}$ solid and the fluid, were perturbed along a marginal direction which is suggested by rigorous work,[35] the resulting line of higher-order transitions would scan effective values of q until joining first-order transitions at[35] exactly $q=4$. Our renormalization is not expected to yield the corresponding line of fixed points, but the topology could be approached. Indeed, by our estimated accuracy, the M_4 exponents $y_2 = 1.489$ and $y_4 = 0.230$ are consistent with the exact values $y_2 = 1.5$ and $y_4 = 0$ demanded by the above scenario. Furthermore, the M_4 exponents are closer to the exponents of M_5, another four-state Potts terminus[36] obtained approximately in our calculation, than to the exponents of M_4'. On the other hand, the point M_4' has its leading exponent y_2 in agreement, within our accuracy, with the conjectured[36] exact multicritical exponent of the three-state Potts lattice gas, and with the approximate multicritical exponent of krypton on graphite, obtained in a larger renormalization calculation.[3]

The measurement of critical exponents can confirm the higher-order melting transitions of commensurate solids exhibited in our phase diagrams. The precise values of these critical exponents are obtained from the exact (rigorous[41,45] or conjectured[47,36]) thermal eigenvalue exponents y_2 and y_4, and from the magnetic eigenvalue exponent $y_1 = \frac{15}{8}$. The latter value appears to be correct for all discrete-spin models in two dimensions.[49,2] Experimentally accessible properties are the specific heat,[7-9] the coverage[5,6] n, and the density difference[10-14] $n_a - n_b$ between two sublattices. The respective critical exponents $\alpha = 2 - d/y_2$, $\beta_{22} = 1 - \alpha = (d - y_2)/y_2$, and $\beta_{12} = (d - y_1)/y_2$ describe power-law singularities, as functions of thermodynamic fields such as temperature T or chemical potential μ. (In these relations, y_2 represents the leading thermal exponent, so that the entry under y_4 in Table I should be used when there is no y_2.) For example, for constant T and μ, respectively,

$$|n - n_0| \sim \begin{cases} |\mu - \mu_0|^{\beta_{22}} , \\ |T - T_0|^{\beta_{22}} , \end{cases} \qquad n_a - n_b \sim \begin{cases} |\mu - \mu_0|^{\beta_{12}} , \\ |T - T_0|^{\beta_{12}} . \end{cases} \tag{11}$$

Along the melting lines of the $\sqrt{3} \times \sqrt{3}$ and 2×2 solids $(\alpha = 1 - \beta_{22}, \beta_{12})$ should be $(\frac{1}{3}, \frac{5}{48})$ and $(\frac{2}{3}, \frac{1}{12})$, respectively. Exponents measured for the $\sqrt{3} \times \sqrt{3}$ melting agree with these values: $\alpha = 0.36 \pm 0.02$ in helium on graphite[8] and $\beta_{12} = 0.09 \pm 0.03$ in krypton on graphite.[11] At the multicritical point M_4' of the $\sqrt{3} \times \sqrt{3}$ solid, these exponents[36] should be $(\frac{5}{6}, \frac{7}{96})$. At the multicritical point M_5 of the 2×2 solid, they should have the same[36] values as at the corresponding melting line, given above. Another exponent is defined at a multicritical point, $\beta_{24} = (d - y_2)/y_4$, for the shape of the coexistence boundary,

$$[n(\text{solid}) - n(\text{fluid})]_T \sim (T_0 - T)^{\beta_{24}} . \tag{12}$$

An exponent β_{24} smaller (larger) than one corresponds to a flat (cusped) coexistence boundary, as at M_4' (as at M_4 and M_5). The same exponent applies to the coverage along the higher-order line close to the multicritical point. Thus, $\beta_{24} < 1$ corresponds to a higher-order line in (n,T) space reaching the multicritical point with zero limiting slope dn/dT. For $\beta_{24} > 1$, the nonsingular background dominates the coverage, and the limiting slope is nonuniversal and, in general, nonzero. [See Sec. III C for a discussion of crossover effects in Fig. 7(l).]

E. Experimental phase diagrams

First, words of caution are appropriate. The quantitative error in our phase diagrams due to the approximate renormalization, estimated from comparison with the exact K_u^* in Table I, seems to be 10 to 15% (see also the zero- and infinite-temperature limits in Sec. III A). Because the phase diagrams change rapidly in the region where J_2 and J_3 are close to equal, they are very sensitive to the specific values of the coupling constants. Thus, a small error of the prefacing could have important effects on the location of a given type of phase diagram. Further, a more careful treatment of physisorption problems relies on an averaging[3] over all positions within the cells of the periodic substrate potential, yielding temperature-dependent lattice-gas couplings, $J_m(T)$, which could be affected by about 10%. It appears that the finite-size effects of the experimental systems, with heterogeneous boundary conditions,[38] extend the regions of effective coexistence.[3] All of these effects will quantitatively distort the global descriptions presented here. More importantly, our present procedure discards, within the partition sum, structures of the adsorbate incommensurate to the substrate.[50] We obtain commensurate ordered structures, which could be preempted by incommensuration in real systems. This seems to be the case for xenon on graphite, for which the Lennard-Jones potential[19] ($\sigma/a = 1.68$) suggests a 2 × 2 solid, whereas x-ray scattering has shown incommensuration.[29]

Neutron scattering from submonolayers of methane physisorbed on graphite indicates the coexistence of a $\sqrt{3} \times \sqrt{3}$ solid and a gas at low temperatures,[30] the coexistence of an expanded incommensurate solid and a gas at intermediate temperatures,[30] the coexistence of a liquid and a gas at higher temperatures,[31] and finally a single hypercritical fluid at the highest temperatures.[31] The boundaries between these four regions seem to occur at constant temperature. If, based on the information on physisorbed xenon,[29] one postulates that the 2 × 2 solid is preempted by incommensuration, the above picture is reproduced by the low coverage portion of our Fig. 6(h) ($\sigma/a = 1.6465$). Further, the experimental boundaries[30,31] are approximately at $kT/\epsilon = 0.34$, 0.48, and 0.59, where we used the Lennard-Jones well depth[51] of $\epsilon = 122$ K. These values generally agree with Fig. 6(h), and can be more accurately reproduced by fine tuning our initial potential. This qualitative comparison suggests that, unlike the monatomic noble gases,[6,19] adsorbed methane has a larger effective hard-core diameter than the bulk value[51] which is $\sigma/a = 1.55$. Presumably, the attraction of the carbon atom to the substrate distorts the surrounding hydrogen tetrahedron.

Finally, Figs. 6(l) and 7(l) [as well as Fig. 8(b)] should be compared with the phase diagram of oxygen chemisorbed on nickel (111), recently studied by low-energy electron diffraction.[33] The latter work has determined a region of 2 × 2 solid, with and without a coexistent fluid, in encouraging qualitative agreement with our results. Namely, this experimentally determined region terminates with a flat boundary at low coverages, and, at higher coverage, a narrow "neck" extends to high temperatures. Further, at still higher coverage, a $\sqrt{3} \times \sqrt{3}$ solid is detected, again in qualitative agreement with our results. The microscopic description of oxygen on nickel (111) is quite similar, but not identical to our starting models. Thus, we hope that a technical modification of our method would make contact with a rich structure revealed by LEED and Monte Carlo work.[33]

ACKNOWLEDGMENTS

We thank G. Dresselhaus, M. S. Dresselhaus, E. M. Hammonds, P. M. Horn, A. R. Kortan, and M. Schick for useful conversations. This work was in part supported by NSF Grants No. DMR77-10210 and No. DMR78-24185, and an IBM Fellowship for A.N.B.

---

*Present address.

[1] M. Schick, J. S. Walker, and M. Wortis, Phys. Lett. A 58, 479 (1976); Phys. Rev. B 16, 2205 (1977).

[2] A. N. Berker, S. Ostlund, and F. A. Putnam, Phys. Rev. B 17, 3650 (1978).

[3] S. Ostlund and A. N. Berker, Phys. Rev. Lett. 42, 843 (1979).

[4] J. G. Dash, *Films on Solid Surfaces* (Academic, New York, 1975).

[5] A. Thomy and X. Duval, J. Chim. Phys. 66, 1966 (1969); 67, 286, 1101 (1970); Y. Larher, J. Chem. Soc. Faraday Trans. 1 70, 320 (1974); J. Chem. Phys. 68, 2257 (1978).

[6] F. A. Putnam and T. Fort, Jr., J. Phys. Chem. 79, 459 (1975); 81, 2164 (1977); F. A. Putnam, T. Fort, Jr., and R. B. Griffiths, *ibid.* 81, 2171 (1977).

[7] M. Bretz and J. G. Dash, Phys. Rev. Lett. 27, 647 (1971); M. Bretz, J. G. Dash, D. C. Hickernell, O. E. McLean, and O. E. Vilches, Phys. Rev. A 8, 1589 (1973); R. L. El-

gin and D. L. Goodstein, *ibid.* 9, 2657 (1974); D. M. Butler, G. B. Huff, R. W. Toth, and G. A. Stewart, Phys. Rev. Lett. 35, 1718 (1975).

[8] M. Bretz, Phys. Rev. Lett. 38, 501 (1977).

[9] T. T. Chung and J. G. Dash, Surf. Sci. 66, 559 (1977); D. M. Butler, J. A. Litzinger, G. A. Stewart, and R. B. Griffiths, Phys. Rev. Lett. 42, 1289 (1979).

[10] J. K. Kjems, L. Passell, H. Taub, and J. G. Dash, Phys. Rev. Lett. 32, 724 (1974); J. K. Kjems, L. Passell, H. Taub, J. G. Dash, and A. D. Novaco, Phys. Rev. B 13, 1446 (1976); W. R. Brooks, Ph.D. thesis (Stevens Institute of Technology, 1977) (unpublished).

[11] P. M. Horn, R. J. Birgeneau, P. Heiney, and E. M. Hammonds, Phys. Rev. Lett. 41, 961 (1978).

[12] C. G. Shaw, Ph.D. thesis (University of Washington, 1979) (unpublished); R. D. Diehl, C. G. Shaw, S. C. Fain, Jr., and M. F. Toney (unpublished).

[13] M. D. Chinn and S. C. Fain, Jr., Phys. Rev. Lett. 39, 146 (1979).

[14] P. W. Stephens, P. Heiney, R. J. Birgeneau, and P. M. Horn, Phys. Rev. Lett. 43,. 47 (1979).

[15] S. Alexander, Phys. Lett. A 54, 353 (1975).

[16] E. Domany, M. Schick, and J. S. Walker, Phys. Rev. Lett. 38, 1148 (1977); E. Domany, M. Schick, J. S. Walker, and R. B. Griffiths, Phys. Rev. B 18, 2209 (1978).

[17] J. S. Walker and M. Schick, Phys. Rev. B 20, 2088 (1979).

[18] B. W. Southern and D. A. Lavis, J. Phys. C 12, 5333 (1979).

[19] R. Wolfe and J. R. Sams, J. Phys. Chem. 69, 1129 (1965).

[20] V. P. Toan and T. Fort, Jr., paper presented at the 52. Colloid and Surface Science Symposium, Knoxville, Tenn., 1979.

[21] A. N. Berker, Phys. Rev. B 12, 2752 (1975).

[22] J. M. J. van Leeuwen, Phys. Rev. Lett. 34, 1056 (1975).

[23] K. G. Wilson, Phys. Rev. B 4, 3174, 3184 (1971).

[24] T. Niemeijer and J. M. J. van Leeuwen, in *Phase Transitions and Critical Phenomena*, edited by C. Domb and M. S. Green (Academic, New York, 1977), Vol. 6.

[25] E. Domany and E. K. Riedel, Phys. Rev. Lett. 40, 561 (1978); Phys. Rev. B 19, 5817 (1979).

[26] R. B. Potts, Proc. Cambridge Philos. Soc. 48, 106 (1952).

[27] A. A. Migdal, Zh. Eksp. Teor. Fiz. 69, 1457 (1975) [Sov. Phys. JETP 42, 743 (1976)].

[28] L. P. Kadanoff, Ann. Phys. (N.Y.) 100, 359 (1976); Rev. Mod. Phys. 49, 267 (1977).

[29] E. M. Hammonds, P. Heiney, P. W. Stephens, R. J. Birgeneau, and P. Horn (unpublished). Also see J. A. Venables, M. Kramer, and G. L. Price, Surf. Sci. 55, 373 (1976); 57, 782(E) (1976) for a transmission electron diffraction study.

[30] P. Vora, S. K. Sinha, and R. K. Crawford, Phys. Rev. Lett. 43, 704 (1979).

[31] J. P. Coulomb, M. Bienfait, and P. Thorel, Phys. Rev. Lett. 42, 733 (1979).

[32] W. -Y. Ching, D. L. Huber, M. G. Lagally, and G. -C. Wang, Surf. Sci. 77, 550 (1978).

[33] A. R. Kortan, P. I. Cohen, and R. L. Park, J. Vac. Sci. Technol. 16, 541 (1979); L. D. Roelofs, T. L. Einstein, P. E. Hunter, A. R. Kortan, R. L. Park, and R. M. Roberts, J. Vac. Sci. Technol. 17, (in press) (1980); A. R. Kortan, Ph.D. thesis (University of Maryland, 1980) (unpublished).

[34] K. Binder and D. P. Landau, Surf. Sci. 61, 577 (1976); B. Mihura and D. P. Landau, Phys. Rev. Lett. 38, 977 (1977).

[35] R. J. Baxter, J. Phys. C 6, L445 (1973).

[36] B. Nienhuis, A. N. Berker, E. K. Riedel, and M. Schick, Phys. Rev. Lett. 43, 737 (1979).

[37] A. N. Berker and M. Wortis, Phys. Rev. B 14, 4946 (1976).

[38] A. N. Berker and S. Ostlund, J. Phys. C 12, 4961 (1979).

[39] L. K. Runnels and L. L. Combs, J. Chem. Phys. 45, 2482 (1966); D. S. Gaunt, *ibid.* 46, 3237 (1967).

[40] (a) Similar behavior involving vacancies within possible commensurate structures has recently been detected in x-ray data on alkali metals intercalated in graphite: S. Y. Leung, C. Underhill, G. Dresselhaus, T. Krapchev, R. Ogilvie, and M. S. Dresselhaus, Solid State Commun. 32, 635 (1979). (b) The phase diagrams of Figs. 6(g), 6(h) present analogies to observations of alkali metals intercalated in graphite, where the coexistence of different commensurate ordered phases is not very unusual. Further, with transmission electron microscopy on stage-2 rubidium, a phase transition is seen as temperature is changed, from the coexistence of one ordered phase and a disordered phase, to the coexistence of another ordered phase and the disordered phase. [N. Kambe, G. Dresselhaus, and M. S. Dresselhaus, Phys. Rev. B 21, 3491 (1980); and private communication.]

[41] L. Onsager, Phys. Rev. 65, 117 (1944); C. N. Yang, *ibid.* 85, 809 (1952).

[42] In fact, $C_{(3)}$ occurs in Figs. 7(c), 7(b) and $C_{(4)}$ occurs in Figs. 6(e)–6(j) and 7(e)–7(j). Another way of phrasing this technical distinction is that the liquid next to the critical point can be either the melted $\sqrt{3} \times \sqrt{3}$ solid, or the melted 2×2 solid.

[43] M. E. Fisher and D. R. Nelson, Phys. Rev. Lett. 32, 1350 (1974). For a magnetic system phase diagram similar to our Fig. 8, see S. Galam and A. Aharony, J. Phys. C (in press) (1980).

[44] A. N. Berker and D. R. Nelson, Phys. Rev. B 19, 2488 (1979).

[45] R. J. Baxter and F. Y. Wu, Phys. Rev. Lett. 31, 1294 (1973); I. G. Enting, J. Phys. A 8, L35 (1975).

[46] L. Mittag and M. J. Stephen, J. Phys. A 7, L109 (1974); D. Kim and R. I. Joseph, J. Phys. C 7, L167 (1974).

[47] M. P. M. den Nijs, J. Phys. A 12, 1857 (1979).

[48] B. Nienhuis and M. Nauenberg, Phys. Rev. Lett. 35, 477 (1975).

[49] M. Suzuki, Prog. Theor. Phys. 51, 1992 (1974).

[50] J. M. Kosterlitz and D. J. Thouless, J. Phys. C 6, 1181 (1973); B. I. Halperin and D. R. Nelson, Phys. Rev. Lett. 41, 121 (1978); D. R. Nelson and B. I. Halperin, Phys. Rev. B 19, 2457 (1979); P. Young, *ibid.* 19, 1855 (1979).

[51] J. O. Hirschfelder, C. F. Curtiss, and R. B. Bird, *Molecular Theory of Gases and Liquids* (Wiley, New York, 1964).

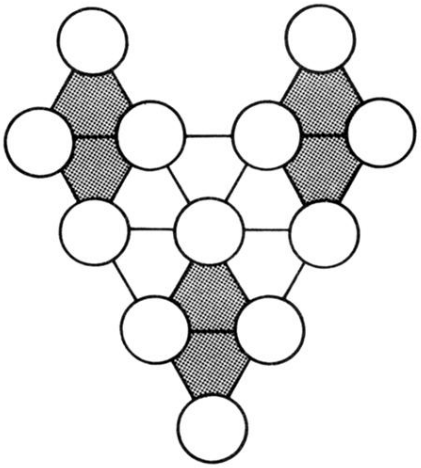

FIG. 3. Group of 12 lattice-gas sites, underlying a single supersite in the prefacing transformation.